High Speed Permanent Magnet Assisted Synchronous Reluctance Machines - Part II: Performance Boundaries

Mauro Di Nardo, *Member, IEEE,* Gianvito Gallicchio, Marco Palmieri, *Member, IEEE,* Alessandro Marfoli,
Michele Degano, *Senior Member, IEEE,* Chris Gerada, *Senior Member, IEEE,*
and Francesco Cupertino, *Senior Member, IEEE*

Abstract—The insertion of permanent magnets (PMs) within the rotor slots of Synchronous Reluctance Machines (SyRM) is the most common design strategy used to increase significantly their performance. In this paper it is shown how a permanent magnet assisted synchronous reluctance machine (PMaSyRM) can be optimized to satisfy all the electromagnetic and structural constraints arising as the maximum operating speed increases. This is done considering a variety PMs material. This work, the second of two companion papers, briefly recalls the novel systematic design approach proposed in Part I, and then describes the characteristics of the optimal machines achieved considering a maximum speed ranging from 1 to 140 krpm with and without the assistance of ferrite and neodymium based PMs. The reasons behind the performance deterioration as the speed increases are all investigated along with the geometrical variations of the optimal designs. The selection of the design solution to be manufactured is justified as well as the final structural and electromagnetic refinement stages leading to the prototype. All the reported considerations are experimentally validated testing an 8.5kW at 80krpm PMaSyRM, comparing the measured and expected performance in terms of torque and internal power factor.

Index Terms—Analytical design, finite element analysis, high speed, iron ribs, permanent magnet, structural rotor design, synchronous reluctance machines.

I. INTRODUCTION

The performance of Synchronous Reluctance Machines (SyRM) can be improved inserting permanent magnets (PMs) within the rotor slots [1]–[3]. When the performance improvement is medium-low, the resulting machine is usually called permanent magnet assisted synchronous reluctance machine (PMaSyRM) otherwise - when dominant - it falls within the realm of the interior permanent magnet synchronous machines [4], [5]. The differentiation between these two machine types is definitely vague and open to interpretation [6], [7]. It can be either related to the torque contribution quotas as stated above or to the design process [8]. In fact, the latter can be performed either designing a SyRM and then adding the PMs with a given criterion or considering both torque contributions at the same time [9] or

considering only the PM torque in the first instance neglecting the reluctance component. When the application involves high speed (HS) operation, the rotor structural requirement becomes more demanding because the needed strengthening iron rib dimensions increase at the cost of a lower torque production [10]. In such cases, the commonly adopted low-speed design practice of supposing a certain saturation level of the iron ribs when estimating both q-axis inductance and PM flux linkage looses accuracy. Indeed, the knowledge of the saturation levels of the iron ribs is fundamental in determining the performance of a HS-PMaSyRM. In addition, the analytical estimation of the cross-saturation phenomena [11]–[13] (which depend also on the iron rib dimension) represents a further design challenge due to the inherent non-linear behavior of the SyRMs. All these aspects have been deeply investigated in the first part of these two companion papers, where a general hybrid analytical-FE design procedure for high speed PMaSyRMs has been introduced and FE-validated. In particular, all the non-linear electromagnetic and structural aspects of the machine behaviour have been considered, fully defining both stator and rotor geometries and calculating the PM dimensions in order to achieve a desired power factor.

The aim of this second part of the study is to use the proposed approach in order to:

- design several machines having different operating speeds ranging from 1 to 140krpm;
- consider the effect of different PM types, e.g. Ferrite and NdFeB magnets, with respect to the SyR designs;
- evaluate the effectiveness of adding the PMs once both stator and rotor geometries are defined;
- analyse how and why the optimal performance changes as the maximum speed increases;
- analyse the optimal geometries obtained considering different speeds, magnet grades and design choices.

To validate the proposed design procedure and outlined general design guidelines, an 8.5kW-80krpm PMaSyRM is manufactured and tested on an instrumented test rig. Prior to prototyping, the rotor of the optimal machine is structurally refined in order to optimize the location and distribution of the iron ribs along the barrier so to ease the assembly process.

In the next section a brief recall of the proposed design procedure is given. Section III discusses how torque and power factor change as the speed increases considering different

M. Di Nardo, A. Marfoli, M. Degano and C. Gerada are with the Power Electronics and Machine Control Group, University of Nottingham, Nottingham, NG7 2GT, UK, email: mauro.dinardo4@nottingham.ac.uk

G. Gallicchio, M. Palmieri and F. Cupertino are with the Department of Electrical Engineering and Information Technology, Politecnico di Bari, Bari, 70126 Italy.

magnet grades for a wide range of design variables. Section IV reports the maximum performance achievable with different magnet types as the speed increases also considering the optimal SyRMs, while section V analyses the optimal geometries. Section VI describes the refinement stages needed before manufacturing the selected design. Last section reports the experimental validation of the machine performance.

II. Brief Recall of Design procedure

The proposed procedure starts from designing a wide range of baseline machines (whose main parameters are shown in Fig. 1) considering null the PM effects and imposing a pre-defined saturation level of the iron ribs as summarized in the flowchart of Fig. 2. Each machine geometry is identified by only two independent per unit design variables, namely split sr and magnetic mr ratio, defined as:

$$sr = \frac{r_r}{r_s}, \quad mr = \frac{B_g}{B_{fe}} \tag{1}$$

where r_r is the rotor radius, r_s the stator outer radius, B_g the airgap flux density and B_{fe} the desired iron flux density. Then, for each design solution, an iterative procedure is implemented in order to size the PMs and the rotor iron ribs and to calculate the q-axis inductance and PM flux linkage. In particular, the procedure consists of the following steps:

1) design the PMs according to a given criterion (e.g. maximum power factor or constant power speed range);
2) mechanically size the iron ribs also considering the PMs weights;
3) verify the dimensions of the iron ribs with the initially supposed ones and iterate the design accordingly;
4) solve the non-linear q-axis equivalent magnetic circuit to calculate the iron ribs saturation;
5) verify the latter with the initially used values and iterate the design accordingly;
6) once converged, calculate both q-axis inductance and PM flux linkage and so all the electromagnetic performances.

Once this iterative procedure is performed for all the considered $sr - mr$ combinations, a small subset of designs (4 machines placed at the corners of the $sr - mr$ plane) is FE-evaluated in order to determine the performance correction coefficients. Extending the latter to the whole design plane

Fig. 2: Flowchart of the hybrid design procedure

allows adjusting the performance estimation of all designs. By doing so all the disregarded aspects and approximations of the analytical design (e.g. cross-saturation and modeling errors) are fully considered as described in the first part of this work and in [14].

III. Effects of PM insertion at increasing speed

The proposed approach has been used to design several PMaSyRMs with increasing maximum speed without and with the permanent magnet assistance. In particular the two most common magnet families have been investigated considering a neodymium-based PM (N42UH) and ferrite one (35H). These three classes of machines will be hereafter called SyR, NDaSyR and FEaSyR, respectively. Table I lists the main constraints and assumptions of this design exercise.

Fig. 1: Stator and rotor parametrization.

TABLE I: Design constraints and assumptions

Parameter	Value	Units
Outer stator radius	30	mm
Stack length	30	mm
Pole pairs	2	/
Airgap thickness	0.3	mm
N° of stator slots	24	/
N° of flux barriers per pole	3	/
Shape of flux barriers	U/I-shaped	/
Stator/rotor materials	JNHF600/35HXT780T	/
Cooling capacity	30	kW/m^2
Iron flux density	1.4	T
Target ipf	0.9	/

A. Torque

Fig. 3 reports the iso-torque loci (T) in the $sr-mr$ plane for 3 mechanical speeds (40, 80 and 120 krpm) and different PM-assistance. The black markers ●, ▶, ■ represent the locations of the maximum torque designs for the SyRMs, FEaSyR and NDaSyR respectively. The white markers ○ in the FEaSyR and NDaSyR graphs are the respective maximum reluctance torque designs. For a given maximum speed, the torque contour and so the maximum torque design location obtained using ferrite magnets do not significantly deviate from the pure SyR one. On the contrary, the constant torque loci of the NDaSyRMs are remarkably different from the respective baseline SyR designs. In particular, the maximum torque designs tend to move towards lower split ratio and higher magnetic ratio with respect to the position of the respective maximum reluctance solutions.

In order to justify this behaviour, the torque components and the main variables affecting their trends are investigated. Fig. 4 and Fig. 5 depict the reluctance (T_{rel}) and the PM torque (T_{PM}) contours of FE- and ND-assisted machines along with the location of the maximum PM, reluctance and total torque designs. As expected, both torque components decrease as the speed increases due to the thicker structural ribs. The reluctance torque decreases due to the higher q-axis inductance while the PM torque decreases due to the higher rotor PM flux leakage. The rate of these two decrements depends on how the rib dimensions and their saturation levels change with the speed. Both quantities depend on the PM types: the rib dimension are affected by the PM mass density, while the rib saturation is affected by the PM residual flux density. From Fig. 4 and 5 it can be deduced that the reluctance torque shows the same qualitative trends within the design plane as the maximum speed increases for both PM types. On the contrary, the PM torque component shows a completely
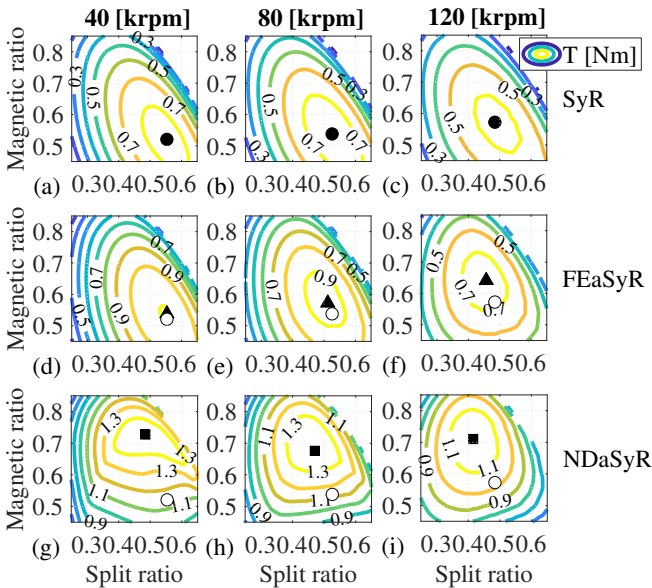
Fig. 3: Torque function of split and magnetic ratio obtained considering three maximum speeds (40, 80, 120 krpm) for the pure SyRM and for the versions assisted by NdFeB and Ferrite magnets.
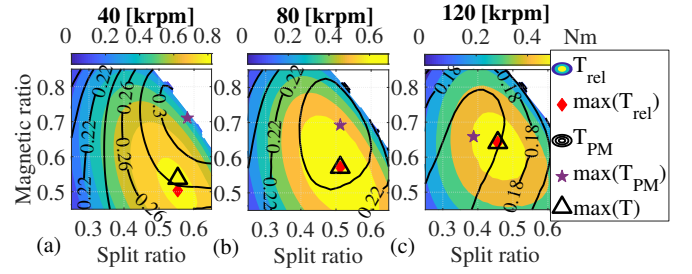
Fig. 4: Reluctance (T_{rel}) and PM (T_{PM}) torque components of the FEaSyRMs as function of both design variables for three different speeds and locations of the maximum reluctance, PM and total torque designs.
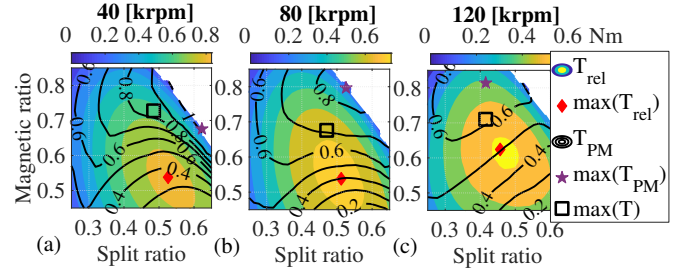
Fig. 5: Reluctance (T_{rel}) and PM (T_{PM}) torque components of the NDaSyRMs as function of both design variables for three different speeds and locations of the maximum reluctance, PM and total torque designs.

different behaviour according to the magnet type. The higher PM torque featured by the NDaSyR machines along with its different contour shape compared to the FEaSyR ones make the total torque contour of NDaSyRMs more affected by the PM-assistance. As a consequence, the maximum torque design when adopting high energy density PM differs from the pure reluctance one and is the compromise between these two torque components. This is clearly evident at 80 krpm and 120 krpm (Fig. 5) while it is not immediate for the 40 krpm case because the PM torque features almost the same maximum value (1 Nm) for several combination of sr and mr of the top right of the design plane.

B. PM torque

The PM torque contours are determined by the d-axis current (independent from the PM material) and by the PM flux linkage (λ_{PM}). The latter depends on the rotor geometry and PM design criterion which in this case is the achievement of a target internal power factor $ipf^* = 0.9$. Adopting this criterion, the PM flux linkage (and so the PM volume V_{PM}) is a nonlinear function of both d- and q-axis inductances, current components and target ipf^*:

$$\lambda_{PM-q}^* = L_q i_q - \lambda_d \left\{ \tan \left[\arctan \left(\frac{i_q}{i_d} \right) - \arcsin \left(ipf^* \right) \right] \right\} \quad (2)$$

The amount of PM (V_{PMs}) required to achieve the desired power factor may exceed the available space within the rotor flux barriers (V_{slots}) if low energy density magnets are adopted or if the target speed is very high (or both); consequently, in
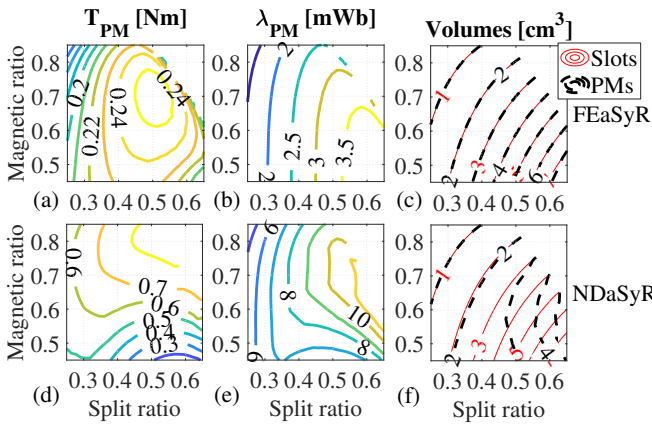
Fig. 6: PM torque (a, d), PM flux linkage (b, e), PM volume and rotor slot volume (c, f) contours in the $sr - mr$ plane when the maximum speed is 80 kprm for both FE- and ND-assisted machines.

Fig. 7: Reluctance torque ratio (a, d), average total rib ratio (b, e), average ribs saturation ratio (c, f) contours in the $sr - mr$ plane when the maximum speed is 80 kprm for both FE- and ND-assisted machines.

such cases, the PM volume would equal the available rotor barriers volume. Fig. 6 reports the PM torque, PM flux linkage, PM volume and available rotor barriers volume in the design plane $sr - mr$ when considering a maximum speed of 80 kprm for both PM types. It can be clearly seen that the PM volume of the FEaSyRMs (Fig. 6c) equals the available rotor barriers space for the considered maximum speed. On the contrary, neodymium based PM allows satisfying the power factor target without exceeding the available space for most of the design plane (Fig. 6f). This justifies the different behaviour of the PM flux, and PM torque, featured by the FE- and ND-assisted machines in the design plane $sr - mr$. Indeed, the PM flux linkage contours of the FEaSyRMs follow the trends imposed by the geometrical constraint of the maximum available space within the rotor barriers, while the NDaSyRMs one follow the trends dictated by the PM design criterion.

C. Reluctance torque

The comparison between the PM-assisted machines and the pure reluctance ones designed for the same maximum speed shows how the adoption of low energy density PM is not convenient also in terms of reluctance torque. The ratio k_{Trel} between the reluctance torque of the PM-assisted machines and the torque of the respective SyRMs (i.e. having equal maximum speed and sr, mr) is higher when adopting neodymium based PM, as shown in Fig. 7a and d for the 80 krpm designs. The reluctance torque ratio between the PM-assisted machines and the pure SyR ones depends on both iron rib dimensions and their saturation levels. The ferrite magnet features a mass density lower than the neodymium one (4600 vs 7500 kg/m^3) which implies a lower increment of the iron rib dimensions with respect to the pure SyRMs. Indeed, the ratio between the average rib sizes (k_{ATB}) of the PMaSyRMs with respect to the SyRMs, shown in Fig. 7b, d) is lower for FEaSyR for a given point in the plane $sr - mr$. Consequently, one would expect the FEaSyRMs to produce higher reluctance torque being smaller the iron rib dimensions. However, when adopting ferrite magnets, the iron ribs saturation is much lower than the neodymium PM one, as shown in Fig. 7c, f) in terms of ratio of the average flux density of the iron ribs. A lower saturation level implies a higher q-axis flux short-circuited
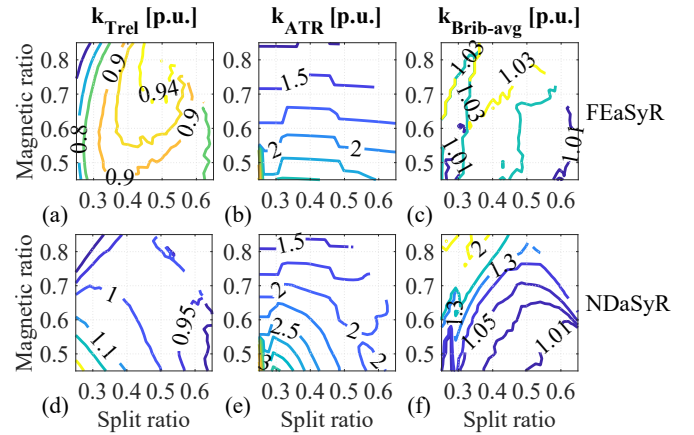
by the iron ribs which in turn determines a higher torque drop. It can be concluded that, although the neodymium-based PMs require bigger iron ribs, they allow to achieve higher rib saturation, therefore the reluctance torque of NDaSyRMs features a lower decrement as the speed increases compared to the FEaSyRMs.

D. Internal power factor

Fig. 8 shows the internal power factor contours for the considered designs. The PM assistance allows increasing this performance index but the target value (0.9) is not achieved for all the solutions of the design plane $sr - mr$. As the design speed increases, the iron rib dimensions increase and this has the twofold effect of worsening the q-axis inductance and reducing the rotor flux barriers area that can accommodate the PM material. In turn, the increment of the q-axis inductance
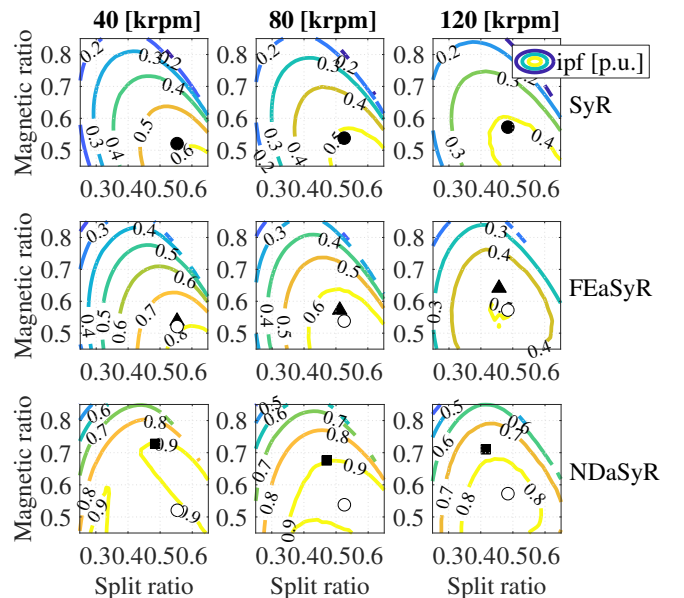
Fig. 8: Internal power factor contour in the $sr - mr$ plane for three different maximum speeds (40, 80, 120 krpm) for the pure SyR and the two PM-assisted versions.
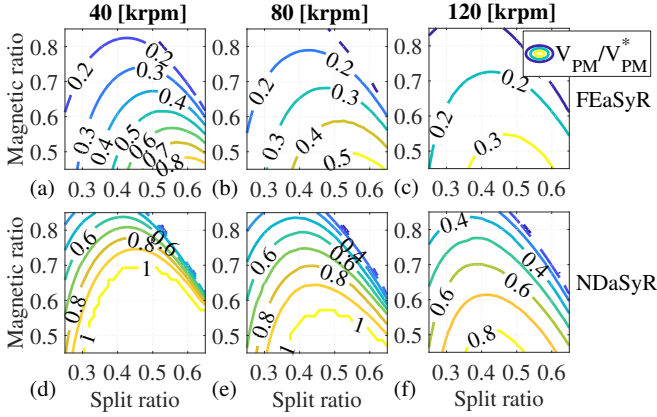
Fig. 9: Ratio between the PM volume (V_{PM}) and its required value (V_{PM}^*) as function of both design variables for three different speeds and for both PM materials.

implies that more PM volume is needed to achieve the target power factor. Therefore, the required amount of PM increases with the speed while the available space decreases. When ferrite magnets are adopted, the target ipf is not reached for none of the considered speeds: in fact, the ratio between the PM volume (V_{PM}) and the required one (V_{PM}^*), shown in Fig. 9, is always lower than one. On the contrary, when using the NdFeB magnets the target power factor is achieved by part of the solutions in the design plane $sr-mr$. The designs featuring an $ipf = 0.9$ correspond to the solutions having the ratio $V_{PM}/V_{PM}^* = 1$. The deviation of the ipf from the target is proportional to the volume ratio V_{PM}/V_{PM}^*.

IV. PERFORMANCE BOUNDARIES

Fig. 10 reports torque and internal power factor of the maximum torque designs (identified by the black markers in Fig. 3 and 8) as a function of the speed obtained after accurate FEA.

As expected, the PM-assistance enhances both performance indexes and the biggest improvement is obtained using high energy density PMs. With neodymium based magnets, the target ipf (0.9) can be achieved up to a certain speed (80 kprm in this case) above which it rapidly decreases reaching 0.7 at 140 krpm. The ipf of the optimal FEaSyRMs is relatively high at low speed (≈ 0.8) and constantly decreases with the speed until it reaches a value similar to the one featured by the optimal SyR design (≈ 0.4) at 140 krpm.
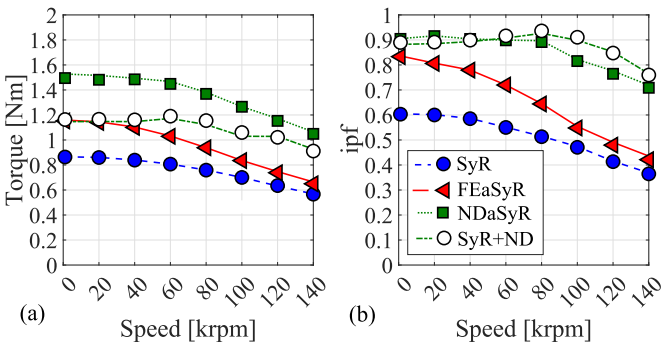
Fig. 10: Torque (a) and internal power factor (b) as a function of the speed of the selected designs.
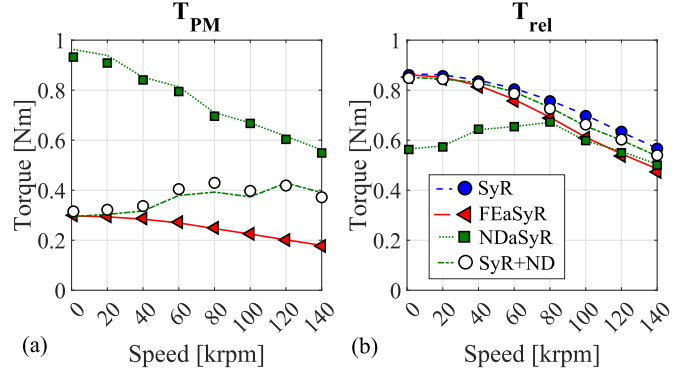
Fig. 11: Permanent magnets (a) and reluctance (b) torque components of the selected machines as function of the speed.

With the adopted PM design criterion, the NDaSyR machines feature an almost doubled torque with respect to the SyRMs for all the considered speed values. Instead, the FEaSyRMs show a lower torque improvement, e.g. around 30% at low speed and 5% at maximum speed, as reported in Fig. 10a.

Along with the pure SyR designs and both PM-assisted variants, Fig. 10 also shows the performance of the PMaSyR machines obtained adding the neodymium based-PM to the maximum reluctance torque design (shown with the white markers ○ in Fig. 3 and 8). These sub-optimal designs, hereafter called SyR+ND, feature power factors similar to those obtained by the optimal NDaSyRMs but with a considerable lower torque (30% lower for the lowest speed design and 5% for the highest one).

Fig. 11 depicts the torque components of all the considered designs as function of the speed. While the PM torque (T_{PM}) of optimal FEaSyR and NDaSyR machines decreases with the speed, their reluctance torque (T_{rel}) shows a different behaviour. Indeed, the reluctance torque component of all PMaSyRMs is lower than the torque of the optimal SyRM designed for the same speed. In particular, T_{rel} decreases with the speed for FEaSyRMs whereas, for NDaSyRMs it is almost constant up to 80 kprm and then reduces reaching 0.45 Nm at 140 kprm. This behaviour is due to two effects: the lower reluctance torque reduction with the speed of the NDaSyRMs as explained in Section III-C and the fact that the distance between the maximum total torque design and reluctance torque design decreases as the speed increases (see markers in Fig. 3g,h,i). It is worth highlighting that the sub-optimal designs SyR+ND feature a higher T_{rel} and a lower T_{PM} compared to the optimal NDaSyRMs.

Fig. 12 reports the mechanical power of all the considered optimal and sub-optimal solutions as function of the maximum design speed. Along with the previous considerations, it is worth to underline that the insertion of PMs within the rotor flux barrier is always beneficial within the considered speed range.

V. ANALYSIS OF THE OPTIMAL MACHINES

Fig. 13 shows the trends of sr and mr of the optimal SyR, FEaSyR, NDaSyR designs as function of the speed. The design variables of the sub-optimal SyR+ND solutions are also
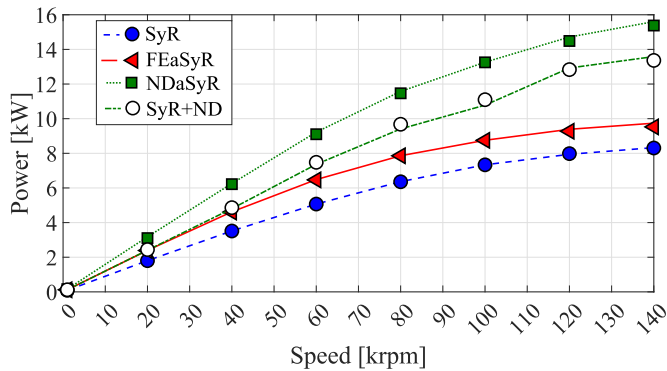
Fig. 12: Power as a function of the speed of the selected designs.

reported and obviously they correspond to SyRMs ones; in fact, their geometries differ from the pure SyR designs only in terms of rib dimensions and PMs. Fig. 14 reports the cross sections of these four classes of machines at 40, 80 and 120 krpm.

The optimal split ratio always decreases with the speed with and without PM assistance and whatever type of PM. Indeed, the designs showing the highest PM and reluctance torques (markers ★, ♦ in Fig. 6, 7) have a decreasing split ratio as the speed increases. Lower sr implies lower centrifugal force which in turn reduces the iron ribs increment and so the reluctance torque drop. Although lower sr implies lower PM flux linkage (due to the lower PM amount, see Fig. 6), the PM torque component increases because the d-axis current increases in the same direction. Another interesting point to underline is that the optimal NDaSyRMs have a lower rotor diameter with respect to SyR and FEaSyRMs. This is due to both higher mass density of the neodymium compared to the ferrite and different contour shapes of the PM torque component for NDaSyRMs and FEaSyRMs.

The optimal magnetic ratio of the SyR and FEaSyR designs tends to increase with the speed because the reluctance torque, which is the main component, increases in the same direction (as shown in Fig. 4). On the contrary, the NDaSyRMs feature an almost constant trend of mr (higher than the FEaSyR one) because the PM torque (which increases with mr) plays a major role in defining the overall torque (Fig. 5). It is then possible to conclude that the optimal NDaSyRMs feature a lower rotor diameter and bigger stator tooth, stator back iron
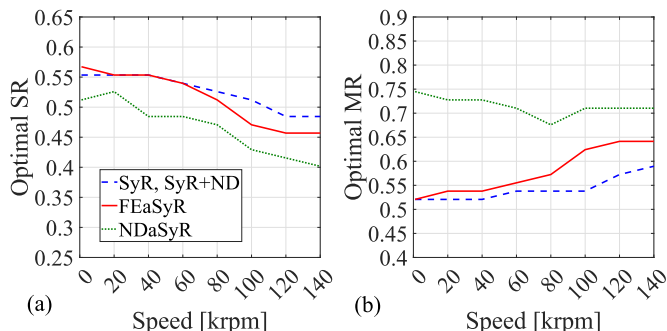
Fig. 13: Design variables sr (a) and mr (b) of the optimal SyR, FEaSyR and NDaSyR machines as function of the speed.
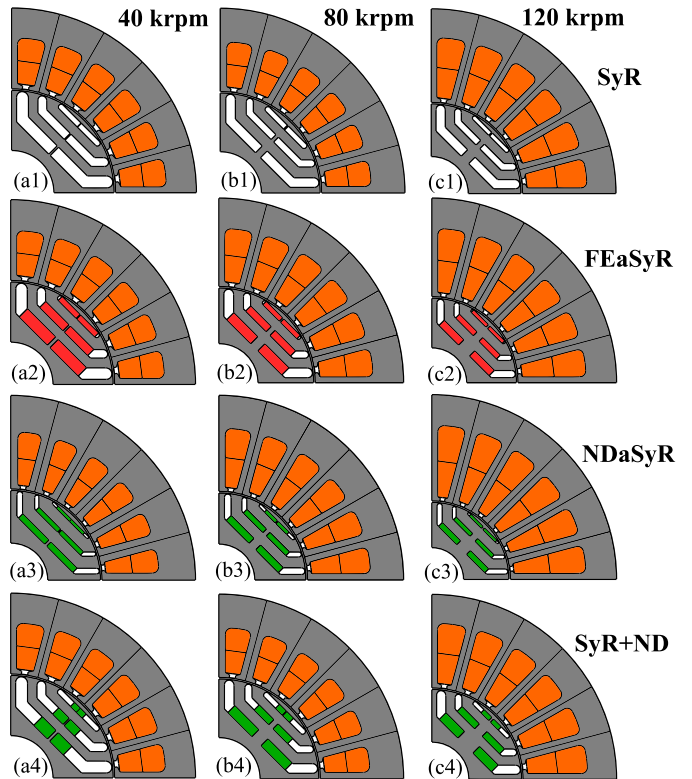
Fig. 14: Cross section of the optimal SyR, FEaSyR and NDaSyR machines and sub-optimal SyR+ND designs at 40, 80 and 120 kprm.

TABLE II: PM volume (V^*_{mag}) of the selected designs [cm^3]

Speed [krpm]	FEaSyR	NDaSyR	SyR+ND
40	5.8	2.6	2.6
80	4.3	2.6	3.4
120	2.7	1.8	3.2

and rotor flux guides with respect to FEaSyRMs, as it can be seen from Fig. 14. Finally, it is worth noticing that above a certain speed (40kprm in this case), the sub-optimal designs SyR+ND make use of more PM material compared to the optimal NDaSyRMs, as shown in Table II.

VI. DESIGN REFINEMENT

The proposed design approach and outlined general design insights have been experimentally validated prototyping and testing an 80 kprm PMaSyRM. Although designing a PMaSyRM first optimizing the reluctance torque and then adding high energy density permanent magnets leads to a sub-optimal design, the solution SyR+ND, shown in Fig. 14b4, has been selected as final candidate to be manufactured and tested. This design solution produces less torque using more magnet material, but it eases the manufacturing of the rotor. Indeed, the optimal NDaSyRM at 80 kprm features rotor flux barrier thicknesses lower than 1 mm. This makes the cutting of the rotor lamination a challenging task when considering standard manufacturing techniques commonly used for low-volume production, e.g electrical discharge machining (EDM) or laser cutting. On the contrary, the sub-optimal SyR+ND design have bigger flux barrier dimensions, therefore the

lamination cutting, the PMs manufacturing and their insertion into the rotor are all simplified. It has to be underlined that this manufacturing challenge is due to the small outer diameter required by the specific application under consideration.

This section describes the design refinements carried out on the selected solution before its manufacturing. In particular, first the structural optimization of the rotor iron ribs distribution is detailed and then the PMs are redistributed within the rotor flux barriers in order to minimize the torque ripple.

A. Structural optimization

The proposed design approach allows fully defining the stator and rotor geometries except for the iron ribs distribution. Indeed, the simplified mechanical formulation, used in the analytical design, estimates only the radial iron rib dimensions and not their distributions along the respective flux barriers. Given the complexity of the rotor structural behaviour, the ribs allocations can only be defined via a structural FE-based study, i.e. either a sensitivity analysis or an optimization. The structural integrity of a PMaSyR is guaranteed only if the rotor maximum von Mises stress σ_{vm}^{max} at the maximum speed is below the yield strength of the lamination material ($\sigma_y = 822$ MPa for the considered rotor material). Unfortunately, this condition is satisfied by several iron rib dimensions and distributions. As a consequence, another criterion needs to be defined in order to select the most performing geometry. A possible solution, first reported in [15] and then in [16], consists in minimizing the iron rib dimensions subject to the constraint on the maximum von Mises stress experienced by the rotor at the highest speed. In this case, a FE-based optimization has been carried out solving the following problem:

$$\begin{aligned} \min \quad & ATR \\ \text{s.t.} \quad & \sigma_{vm}^{max} \le k_s \cdot \sigma_y \end{aligned} \quad (3)$$

where k_s is a safety factor (0.8), while ATR:

$$ATR = \frac{1}{n} \sum_{i=1}^{n} (2 \cdot TR^i + 2 \cdot LR^i + CR^i) \quad (4)$$

is the average total rib of the n flux barriers, being TR^i, CR^i and LR^i the tangential, central and lateral rib sizes, all depicted in Fig. 15a. It is worth to underline that during the structural FE optimization the flux barrier heights h_a^i and their angular positions at the airgap $\Delta\alpha^i$, reported in red in Fig. 15a,
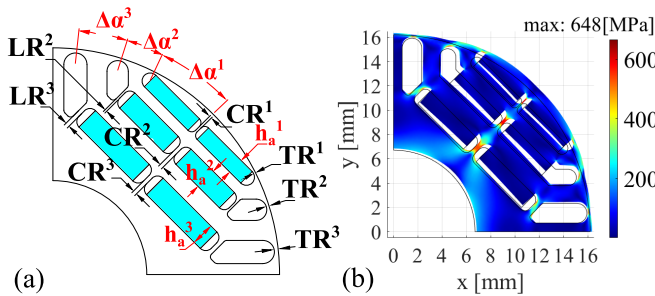
Fig. 15: a) Full rotor parametrization, b) Von Mises stress distribution of the optimal at 80krpm.

are kept constant to the respective values obtained with the proposed hybrid design procedure.

Solving this constrained one-objective optimization problem (3), involving 8 geometrical variables to identify, indirectly leads to the solution featuring the highest possible torque for a given stress limit ($k_s \cdot \sigma_y$). The adoption of this structural design approach lies on two hypotheses. Indeed, the decrement of the average torque caused by the increment of an iron rib has to be independent from its position (which can be either on the tangential, lateral, or central rib). Secondly, the iron rib dimensions and their distribution should have a negligible effect on the torque ripple. Although the first hypothesis can be considered always verified, the second is definitely a strong assumption and needs to be verified case by case. Both these two aspects will be investigated in the next sub-section.

The problem (3) has been solved using a stochastic optimization algorithm (differential evolution) with 80 elements evolving for 150 generations. In order to obtain the most conservative design, the structural optimization has been carried out considering the flux barriers fully filled of PMs, even though the initial solution (Fig. 14b4) has lower PM material in the two outermost rotor slots. A minimum rib thickness of 0.1 mm has been considered during the optimization as manufacturing constraint; both central and lateral ribs are not drawn if their optimal values fall below this threshold.

Fig. 15b reports the Von Mises stress distribution of the optimal rotor geometry while Table III lists its iron rib dimensions. As expected, the optimal geometry features increasing central ribs from the outermost to the innermost barrier. However, this does not hold true for the tangential ribs as the optimal geometry does not have the lateral ribs on the middle barrier. It is worth underlining that the total rib per flux barrier along with their average obtained with the structural FE optimization are similar to the respective values analytically estimated with the proposed design methodology as reported in Table III.

TABLE III: Iron ribs dimensions of the optimal design [mm]

Flux barrier	TR	CR	LR	total	total analytical
1	0.33	0.20	-	0.86	0.43
2	0.57	0.37	-	1.51	1.3
3	0.30	0.51	0.55	2.21	2.4
ATR				1.52	1.38

B. PM redistribution analysis

The average total ribs (ATR) obtained with the structural optimization is slightly higher than the expected one as shown in Table III. As a consequence, the average torque of the mechanical optimized design is lower than the expected value albeit it is less than 5% at the MTPA (Maximum torque per Ampere) condition as shown in Fig. 16a. This figure reports both average torque and torque ripple for the rated current as function of the current phase angle. The torque oscillation of both analytical design and structural optimized one is above 20%. This is caused by several phenomena not included in the design workflow such as the local saturation effects and the influence of having different tangential ribs thicknesses. With the aim of reducing the torque pulsation, an
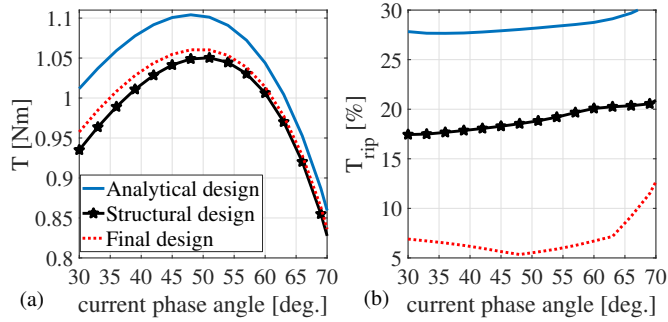
Fig. 16: Average torque and torque ripple as function of the current phase angle for the electromagnetic optimum geometry, the structural one, and the final prototype.

electromagnetic FE sensitivity analysis has been performed redistributing the PMs within the rotor flux barriers keeping unchanged the overall PM volume (equal to the optimal value V_{mag}^* analytically obtained and reported in Table II). Fig. 17 reports the results of such analysis in terms of PM volume placed in the outermost barrier (V_{mag1}), average torque and torque ripple as function of the PM volumes placed in the two innermost rotor barriers (V_{mag2}, V_{mag3}). The PM volumes are expressed in per unit of the respective maximum volumes. Obviously, as both V_{mag2}, V_{mag3} increase, V_{mag1} (Fig. 17a) decreases until it reaches zero when $V_{mag2} = V_{mag3} = 1$ since $V_{mag1} + V_{mag2} + V_{mag3} = V_{mag}^*$. As expected, the average torque maximum variation is less than 3% being the total PM volume kept constant during the analysis (Fig. 17b). On the contrary, the torque ripple changes significantly with the PM distributions (Fig. 17c) and the maximum range of variation is about 20%. In particular, the structural optimized solution (shown with the marker ★) features a torque ripple at the rated MTPA condition of 20% while the minimum torque ripple PM distribution is about 5.2% (red marker ○). The performance of the solution featuring the lowest torque ripple are also reported in Fig. 16 (labeled as Final design).

While the average torque variation between the optimal structural design and the final one is negligible, the torque ripple is significantly improved over a wide range of current phase angle and not only at the MTPA condition. The optimal PM distribution is characterized by an empty outermost barrier and two fully filled innermost barriers. This PM allocation further facilitates their insertion being the outermost slot the
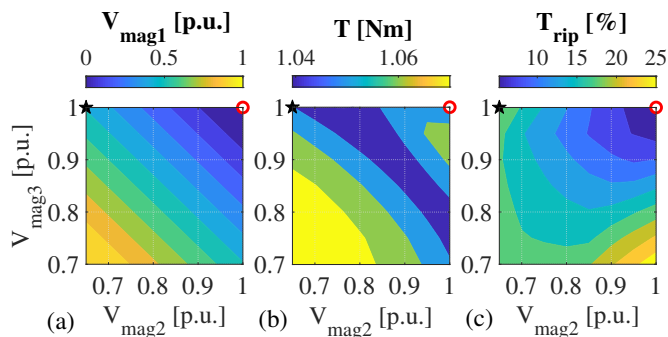
Fig. 17: PM re-distribution FE analysis: a) PM volume of the outermost PM, b) average torque, and c) torque ripple as function of the per unit PM volumes placed in the two innermost flux barriers.
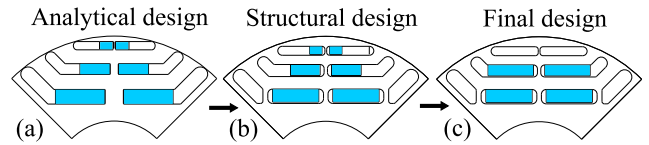
Fig. 18: Design refinement evolution.

smallest one. For the sake of clarity, Fig. 18 shows the rotor geometries and PM distributions obtained with the proposed analytical design methodology (a), after the FE structural optimization (b) and after the PM redistribution FE sensitivity analysis (c).

VII. EXPERIMENTAL VERIFICATION

The final design obtained as described in the previous sections has been prototyped and tested on an instrumented test rig.

A. Prototype and test rig setup

Both stator and rotor were manufactured by EDM and Fig. 19 shows two top view photos of the rotor lamination stack before and after the magnets and shaft insertion. The stator and rotor were assembled into custom designed housing featuring a single spiral water jacket and the inlet and outlet channels for the air-oil mist bearings lubrication, as can be seen on the right side of Fig. 20. The prototyped machine was then coupled, via a gearbox (ratio 1:5.975) and a 3.5 Nm torque sensor, to a load motor (37 kW - 20 krpm Induction motor) supplied by a four-quadrant regenerative drive as shown in Fig. 20. An in-house designed three-phase full-bridge converter featuring SiC power modules was adopted to supply the machine under test [17]. The control platform used to implement the control algorithm is based on a Xilinx Zynq7020 SoC [18].

B. Test results

The first experiment carried out on the prototype is a series of generating no load tests at various speeds aimed at measuring the back electromotive force (bemf). Fig. 21 reports a screenshot of the scope during the no-load voltage test at 24 krpm while Fig. 22 compares the measured and FE-predicted bemf profiles. A good match is evident although small discrepancies are present mainly due to the different behaviour of the tangential iron ribs. Indeed, a small variation of their sizes due to the manufacturing tolerances causes a
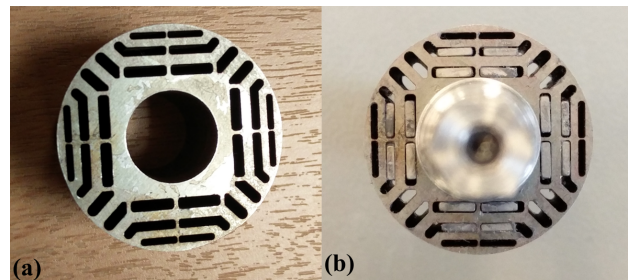
Fig. 19: Top view of the rotor lamination stack before (a) and after (b) magnets and shaft insertion.
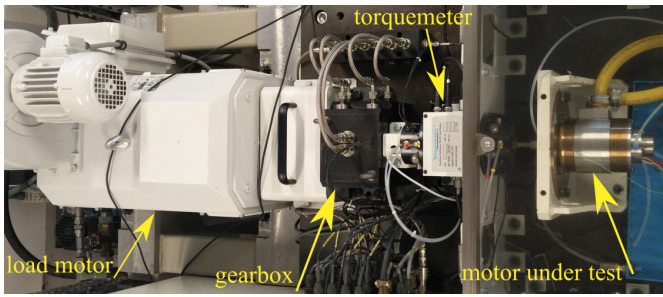
Fig. 20: Experimental setup layout.

different saturation levels and so a discrepancy between the expected and measured voltage profiles.

To confirm the FE-calculated performance, the torque and the internal power factor have been measured implementing the procedure presented in [19]. Fig. 23 reports the results of this series of experimental tests carried out for several current modules and current phase angles. A satisfactory agreement with the FE prediction is clearly visible, although the measured torque is 5% lower when considering a light overload at MTPA condition (i.e. current amplitude 30 A in Fig. 23). Also the internal power factor at the rated MTPA operating point is slightly lower than expected, i.e. 0.8 instead of 0.845. These small discrepancies can be ascribed to the effects that the manufacturing tolerances have on the performance of a small scale prototype.

After measuring the torque and inductances along the maximum torque per ampere trajectory, the PI regulators of a standard vector control scheme [20] can be tuned. After some preliminary tests, several motoring no-load tests have
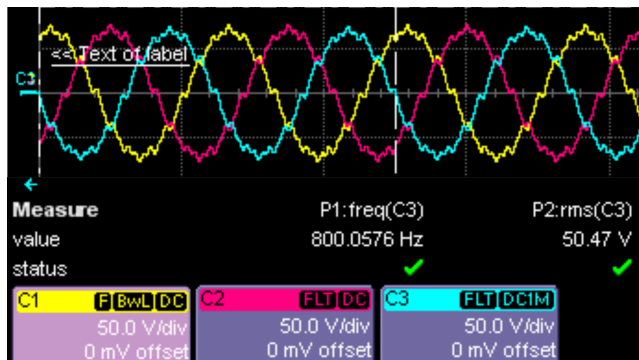
Fig. 21: Scope capture while measuring the phase-to-phase voltages during the no-load test at 24 krpm.
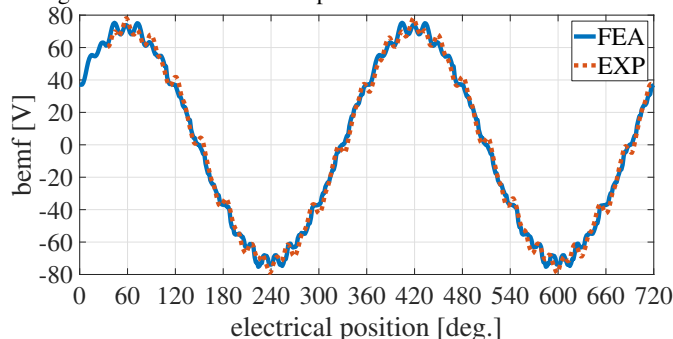
Fig. 22: Comparison between measured and FE phase-to-phase no-load voltages at 24 kprm.
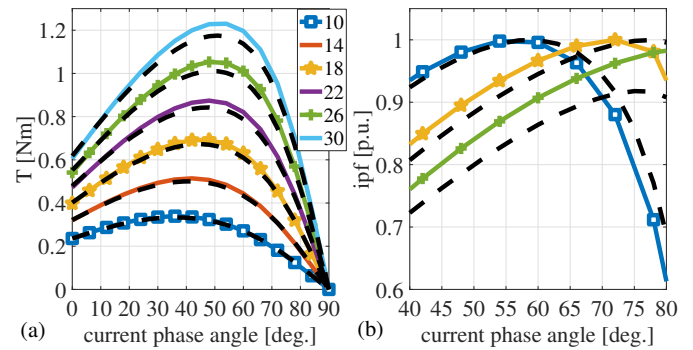
Fig. 23: Comparison between estimated (colored lines) and measured (dashed black lines) average torque (a) and internal power factor (b) as function of the current phase angle and for different peak current amplitudes.
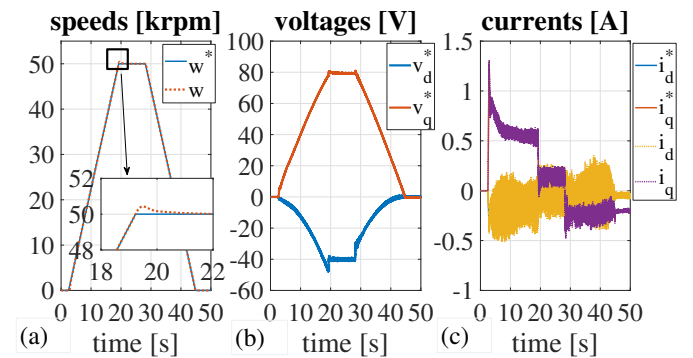
Fig. 24: Motoring no load test up to 50 krpm: a) speed, b) voltages, c) currents.
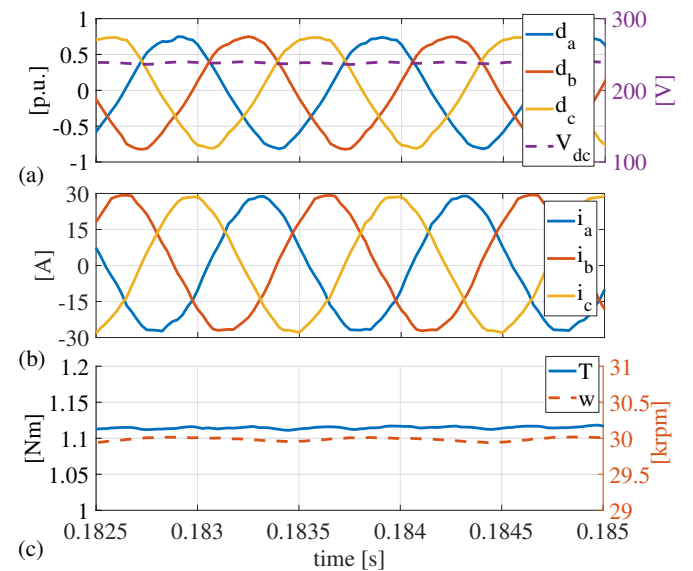
Fig. 25: Load test at 30 krpm and the rated torque: a) duty cycles and dc-link voltage, b) phase currents, and c) torque and speed, all acquired with the control platform at 40 kHz.

been performed imposing a trapezoidal speed reference with increasing maximum values. Fig. 24 reports the measured and the reference speed, d- and q-axis currents and reference voltages during a no-load test up to 50 krpm. After verifying the safe operations up to a certain speed, several load tests have been performed and Fig. 25 shows the duty cycles, dc-link voltage, speed, torque and phase currents all acquired
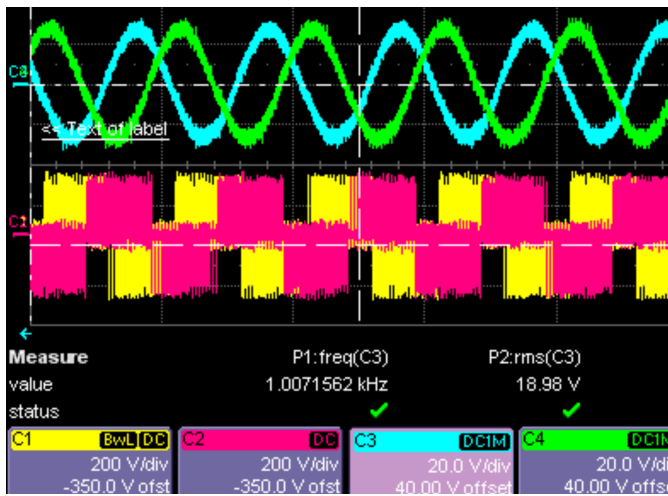
Fig. 26: Scope capture while measuring the phase-to-phase voltages and phase currents during the rated load test at 30 krpm.

with the control platform during the test at the rated torque at 30 krpm. The phase currents and phase-to-phase voltage profiles captured with the scope during the same test are shown in Fig. 26. Above 50 and 30 krpm at no load and load respectively, the measured vibrations exceed the acceptable limits and, for the sake of safety, tests at higher speed have not been performed. The analysis of the vibration spectrum at no load and different rotating speeds allows concluding that a shaft misalignment (or a non-perfect bearings assembly within their housings) is the most probable cause of this unexpected behaviour.

VIII. Conclusion

This work has presented a wide comparative design exercise using a novel design approach for high speed permanent magnet assisted synchronous reluctance machine described in the first part of this work. Indeed, considering all the complexities and non-linearities involved in the relationship between performance and geometry, this paper has shown the design of several machines having maximum speeds ranging from 1 to 140 krpm with different permanent magnet types.

It has been shown that, for a given maximum speed, the maximum torque solution when adopting ferrite PM is geometrically similar to the maximum reluctance torque design. On the contrary, adopting high energy density PM, the maximum total torque design differs from the maximum reluctance one. This difference is mainly due to the bigger PM torque component obtained with neodymium based PMs and its different behaviour in terms of split and magnetic ratio dependencies.

As a consequence, if neodymium based PMs are chosen, the selection of the optimal design (torque-wise) should consider both PM and reluctance torque components. In other words, the design procedure of adding neodymium-PM to the maximum reluctance torque design leads to a sub-optimal solution (i.e. 30% lower output power in the considered case study).

In order to validate the design considerations, an 8.5kW-80kprm NdFeB-PM-assisted synchronous reluctance machine has been prototyped and tested. Both structural and electromagnetic design refinement stages prior the manufacturing

have been fully detailed justifying all the design choices. The prototype has been fully tested up to 50 krpm at no load and up to 30 krpm at load in both generating and motoring operating modes. No-load voltage profile at a fixed speed, average torque and internal power factor as function of current module and phase angle have all been compared to the respective predicted values. Such comparison shows an acceptable agreement endorsing both design methodology and general considerations.

References

[1] Michele Degano, Mukhammed Murataliyev, Wang Shuo, Davide Barater, Giampaolo Buticchi, Werner Jara, Nicola Bianchi, Michael Galea, and Chris Gerada. Optimised design of permanent magnet assisted synchronous reluctance machines for household appliances. *IEEE Transactions on Energy Conversion*, 36(4):3084–3095, 2021.

[2] Won-Ho Kim, Kwang-Soo Kim, Seung-Joo Kim, Dong-Woo Kang, Sung-Chul Go, Yon-Do Chun, and J. Lee. Optimal pm design of pma-synrm for wide constant-power operation and torque ripple reduction. *IEEE Transactions on Magnetics*, 45(10):4660–4663, 2009.

[3] S. Morimoto, M. Sanada, and Y. Takeda. Performance of pm-assisted synchronous reluctance motor for high-efficiency and wide constant-power operation. *IEEE Transactions on Industry Applications*, 37(5):1234–1240, 2001.

[4] Nicola Bianchi, Emanuele Fornasiero, and Wen Soong. Selection of pm flux linkage for maximum low-speed torque rating in a pm-assisted synchronous reluctance machine. *IEEE Transactions on Industry Applications*, 51(5):3600–3608, 2015.

[5] Haiwei Cai, Bo Guan, and Longya Xu. Low-cost ferrite pm-assisted synchronous reluctance machine for electric vehicles. *IEEE Transactions on Industrial Electronics*, 61(10):5741–5748, 2014.

[6] Thanh Anh Huynh and Min-Fu Hsieh. Comparative study of pm-assisted synrm and ipmsm on constant power speed range for ev applications. *IEEE Transactions on Magnetics*, 53(11):1–6, 2017.

[7] Gianmario Pellegrino, Alfredo Vagati, Barbara Boazzo, and Paolo Guglielmi. Comparison of induction and pm synchronous motor drives for ev application including design examples. *IEEE Transactions on Industry Applications*, 48(6):2322–2332, 2012.

[8] Chao Lu, Simone Ferrari, and Gianmario Pellegrino. Two design procedures for pm synchronous machines for electric powertrains. *IEEE Transactions on Transportation Electrification*, 3(1):98–107, 2017.

[9] N. Bianchi and H. Mahmoud. An analytical approach to design the pm in pmarel motors robust toward the demagnetization. *IEEE Transactions on Energy Conversion*, 31(2):800–809, 2016.

[10] C. Babetto, G. Bacco, and N. Bianchi. Synchronous reluctance machine optimization for high-speed applications. *IEEE Transactions on Energy Conversion*, 33(3):1266–1273, 2018.

[11] P. Guglielmi, M. Pastorelli, and A. Vagati. Impact of cross-saturation in sensorless control of transverse-laminated synchronous reluctance motors. *IEEE Transactions on Industrial Electronics*, 53(2):429–439, 2006.

[12] Damiano Mingardi, Mattia Morandin, Silverio Bolognani, and Nicola Bianchi. On the proprieties of the differential cross-saturation inductance in synchronous machines. *IEEE Transactions on Industry Applications*, 53(2):991–1000, 2017.

[13] Angelo Accetta, Maurizio Cirrincione, Maria Carmela Di Piazza, Giuseppe La Tona, Massimiliano Luna, and Marcello Pucci. Analytical formulation of a maximum torque per ampere (mtpa) technique for synrms considering the magnetic saturation. *IEEE Transactions on Industry Applications*, 56(4):3846–3854, 2020.

[14] G. Gallicchio, M. Di Nardo, M. Palmieri, A. Marfoli, M. Degano, C. Gerada, and F. Cupertino. High speed synchronous reluctance machines: Modeling, design and limits. *IEEE Transactions on Energy Conversion*, 37(1):585–597, 2022.

[15] M. D. Nardo, G. L. Calzo, M. Galea, and C. Gerada. Design optimization of a high-speed synchronous reluctance machine. *IEEE Transactions on Industry Applications*, 54(1):233–243, 2018.

[16] A. Credo, G. Fabri, M. Villani, and M. Popescu. Adopting the topology optimization in the design of high-speed synchronous reluctance motors for electric vehicles. *IEEE Transactions on Industry Applications*, 56(5):5429–5438, 2020.

[17] Giovanni Lo Calzo, Pericle Zanchetta, Chris Gerada, Alberto Gaeta, and Fabio Crescimbini. Converter topologies comparison for more electric aircrafts high speed starter/generator application. In *2015 IEEE Energy Conversion Congress and Exposition (ECCE)*, pages 3659–3666, 2015.

[18] A. Galassini, G. Lo Calzo, A. Formentini, C. Gerada, P. Zanchetta, and A. Costabeber. ucube: Control platform for power electronics. In *2017 IEEE Workshop on Electrical Machines Design, Control and Diagnosis (WEMDCD)*, pages 216–221, 2017.

[19] Eric Armando, Radu Iustin Bojoi, Paolo Guglielmi, Gianmario Pellegrino, and Michele Pastorelli. Experimental identification of the magnetic model of synchronous machines. *IEEE Transactions on Industry Applications*, 49(5):2116–2125, 2013.

[20] Thomas M. Jahns, Gerald B. Kliman, and Thomas W. Neumann. Interior permanent-magnet synchronous motors for adjustable-speed drives. *IEEE Transactions on Industry Applications*, IA-22(4):738–747, 1986.

Mauro Di Nardo (M'18) received the M.Sc. (Hons.) degree in electrical engineering from the Polytechnic University of Bari, Italy, in 2012, and the Ph.D. degree in electrical machine design from the University of Nottingham, U.K., in 2017. From 2017 to 2019, he was Head with the AROL R&D Team within the Polytechnic University of Bari leading industrial projects on electrical drives design for mechatronics applications.

Since the 2019, he is with the Power Electronics and Machine Control Group of the University of Nottingham as Research Fellow working on wide variety of projects. His research interests include the analysis, modelling, and design optimizations of permanent magnet and synchronous reluctance machines for automotive, aerospace and household sectors, induction motor for industrial applications as well as niche machine topologies such as bearingless and hysteresis motor.

He has been serving as an Associate Editor for the Open Journal of Industry Applications since March 2021.

Gianvito Gallicchio received the B.Sc. (Hons.) and M.Sc. (Hons.) degrees in electrical engineering from the Politecnico di Bari, Bari, Italy, in 2016 and 2018, respectively. He is currently working toward the Ph.D. degree with the Electrical Machines and Drives Group, Politecnico di Bari, Bari, Italy.

His main research interests include the design and analysis of permanent magnet and synchronous reluctance machines for both traction and high-speed applications, as well as the analysis, modeling and optimization of magnetic couplings.

Marco Palmieri received the M.Sc. and Ph.D. degrees in electrical engineering from Politecnico di Bari, Bari, Italy, in 2011 and 2016, respectively. Since 2017 he has been with the Department of Electrical and Information Engineering, Politecnico di Bari, where he is currently a post-doc researcher.

From 2011 to 2015, he was with the Energy Factory Bari Research Team, working on high-speed electrical machines for aeronautical applications. In 2014 he joined the Power Electronics, Control, and Machines Research Group of the University of Nottingham, working on electrical machines for aeronautical applications. In 2019 he was visiting researcher with the Laboratory of Actuation Technology of the Saarland University. His research interests include the design of high-speed electrical machines by means of optimization algorithms and finite element analysis.

Dr. Palmieri co-received the Prize Paper Award from the IEEE Industrial Electronics Society Electrical Machines Committee in 2015.

Alessandro Marfoli received the M.Sc. in Electrical Engineering from the University of Pisa, Italy, in 2015 and the Ph.D. degree in electrical machine design from the University of Nottingham (UK) in 2020. He is currently a Research Fellow within the same institution working on wide variety of projects of high industrial and scientific impacts.

His main research interests involves the modelling, analysis and optimization of electrical machines including induction and synchronous machines also for bearingless applications.

Michele Degano (SM'21) received his Master's degree in Electrical Engineering from the University of Trieste, Italy, in 2011, and his Ph.D. degree in Industrial Engineering from the University of Padova, Italy, in 2015. Between 2014 and 2016, he was a postdoctoral researcher at The University of Nottingham, UK, where he joined the Power Electronics, Machines and Control (PEMC) Research Group. In 2016 he was appointed Assistant Professor in Advanced Electrical Machines, at The University of Nottingham, UK. He was promoted Associate Professor in 2020.

His main research focuses on electrical machines and drives for industrial, automotive, railway and aerospace applications, ranging from small to large power.

He is currently the PEMC Director of Industrial Liaison leading research projects for the development of hybrid electric aerospace platforms and electric transports.

Chris Gerada (SM'12) is an Associate Pro-Vice-Chancellor for Industrial Strategy and Impact and Professor of Electrical Machines. His principal research interest lies in electromagnetic energy conversion in electrical machines and drives, focusing mainly on transport electrification. He has secured over £20M of funding through major industrial, European and UK grants and authored more than 350 referred publications. He received the Ph.D. degree in numerical modelling of electrical machines from The University of Nottingham, Nottingham, U.K., in 2005. He subsequently worked as a Researcher with The University of Nottingham on high-performance electrical drives and on the design and modelling of electromagnetic actuators for aerospace applications. In 2008, he was appointed as a Lecturer in electrical machines; in 2011, as an Associate Professor; and in 2013, as a Professor at The University of Nottingham. He was awarded a Research Chair from the Royal Academy of Engineering in 2013.

Prof. Gerada served as an Associate Editor for the IEEE Transactions on Industry Applications and is the past Chair of the IEEE IES Electrical Machines Committee.

Francesco Cupertino (M'08–SM'12) received the Laurea and Ph.D. degrees in electrical engineering from the Politecnico di Bari, Bari, Italy, in 1997 and 2001, respectively. Since 2001, he has been with the Department of Electrical and Information Engineering, Politecnico di Bari, Bari, Italy, where he is currently a Full Professor of converters, electrical machines, and drives.

He is the Scientific Director of four public/private laboratories at Politecnico di Bari that enroll more than 50 researchers; the laboratory Energy Factory Bari, with GE AVIO, aimed at developing research projects in the fields of aerospace and energy; the More Electric Transportation laboratory, with CVIT SpA (BOSCH Group), aimed at developing technologies for sustainable mobility; Cyber Physical Systems AROL Bari, with AROL SpA, focused on closure systems for food and beverage; Innovation for Mills, with Casillo Group and Idea75, focused in the Industry4.0 applications for wheat processing. He has authored or coauthored more than 130 scientific papers on these topics. His research interests include the design of synchronous electrical machines, motion control of high performances electrical machines, applications of computational intelligence to control, and sensorless control of ac electric drives.

Dr. Cupertino was the recipient of two Best Paper Awards from the Electrical Machines Committee of the IEEE Industry Application Society and from the homonymous Committee of the IEEE Industrial Electronics Society, in 2015.

He is currently the rector of Politecnico di Bari.